Materials Science and Engineering B 313 (2025) 117908

Contents lists available at ScienceDirect

Materials Science & Engineering B

journal homepage: www.elsevier.com/locate/mseb

Passive RFID Multi-Dimensional sensor for monitoring Light, Humidity, and ethanol

Bairui Tao [a,1,*], Linxin Dong [a,1], Fengjuan Miao [a,*], Xiao Liang [a,*], Paul K. Chu [b]

[a] College of Communications and Electronics Engineering, Qiqihar University, Heilongjiang 161006, China
[b] Department of Physics, Department of Materials Sciences and Engineering, and Department of Biomedical Engineering, City University of Hong Kong, Tat Chee Avenue, Kowloon, Hong Kong, China

ARTICLE INFO

Keywords:
RFID antenna sensor
Nanocomposites
Low cost
Multidimensional sensor

ABSTRACT

RFID technology has matured significantly and plays a crucial role in industrial automation. In breweries, precise monitoring and control of environmental data are required at various stages of the brewing process, including humidity, light exposure, and alcohol concentration during fermentation. To facilitate the monitoring of multiple environmental parameters in complex production environments, a passive RFID multidimensional sensor is designed to cater to brewery automation. The sensor is composed of a tri-frequency ELC resonator antenna designed by HFSS simulation. The passive RFID multidimensional sensor operates stably under ambient conditions for light intensity from 9.7 to 39.1 klx, humidity from 20 % to 80 % RH, and ethanol concentration from 0 to 1,800 ppm. In an environment with light intensity between 9.7 and 39.1 klx, the amplitude change is 20 dB, sensitivity is 0.67 dB/klx, and response time is 15.1 ± 0.7 s. In the RH range of 20–80 %, the measured frequency shift is 0.16 GHz, sensitivity is 2 MHz/%RH, and response time is 6.4 ± 0.5 s. For ethanol concentrations between 0 to 1800 ppm, the amplitude change is 17.9 dB, sensitivity is 0.01 dB/ppm, and response time is 25.1 ± 1.2 s. This sensor is economical while boasting zero power consumption, fast response, excellent stability, and good accuracy. It has large potential in multi-parameter monitoring, especially breweries, by offering stable quality and enhancing the production efficiency.

1. Introduction

With the advancement of RFID technology, more factories are embracing automated production, and breweries are no exception. In the realm of automated production, the brewing process necessitates meticulous control of data related to various brewing environments to ensure the consistent quality of automated-produced products. Traditional brewing methods have become insufficient due to the lack of automation and low efficiency. In the industrial setting, environmental parameters require manual sampling and monitoring to ensure product quality, but it is impacted by the limited intermittent environmental data and monitoring during production. The integration of multiple-parameter RFID sensors is inefficient, costly, hard to control, and power-consuming [1]. Hence, there is a growing demand for intelligent RFID solutions that are both cost-effective and versatile [2].

Different types of RFID sensors are available for environmental detection such as temperature [3,4], humidity [5,6], light intensity [7,8,9], carbon dioxide levels [10,11], pressure [12], as well as health parameters [13,14,15] including vibration [16], tension [17], liquid-level [18], and the monitoring of specific gases in special working environments is important to factories [19,20]. However, many RFID sensors are relatively expensive, and most of them are designed to measure only one or two parameters [21]. In order to measure multiple parameters in complex environments, a common approach involves integrating multiple sensors through circuitry and employing programmed algorithms for unified monitoring [22]. Although integrated solutions offer flexibility, they come with substantial costs and often require batteries to operate. In this respect there are sensors capable of simultaneously monitoring humidity and temperature [23] with reduced costs while offering stable operation. In addition, wearable sensors for monitoring bodily parameters [24] can be battery-free, portable, and compact patch-like thus offering safe and cost-effective solutions. Furthermore, sensors based on ELC resonators [25,26] are known for their simple design, easy fabrication, and lower costs.

* Corresponding authors.
E-mail addresses: Tbr_sir@163.com (B. Tao), miaofengjuan@163.com (F. Miao), 584721679@qq.com (X. Liang).
[1] Bairui Tao and Linxin Dong are co-first authors.

https://doi.org/10.1016/j.mseb.2024.117908
Received 7 October 2024; Received in revised form 1 December 2024; Accepted 3 December 2024
Available online 6 December 2024

To facilitate cost-effective monitoring of multiple environmental parameters, a passive RFID multidimensional sensor is designed for high stability and rapid response. It monitors three parameters: light intensity, humidity, and ethanol concentration in air thus rendering it desirable for breweries. The design and performance are optimized by simulations using the HFSS software. The antenna model is then translated into a printed circuit board (PCB) for antenna fabrication to ensure simple and cost-effective production. This approach enables simultaneous monitoring of light intensity, humidity, and ethanol concentration. By precisely controlling the brewing time and maintaining the optimal environmental conditions, this sensor contributes to the stability and efficiency of brewing processes and improves the quality of the products.

2. Antenna simulation and fabrication

2.1. Design principles

The RFID sensor without a chip is a multi-frequency antenna composed of several differently sized ELC resonators and microstrip lines. To measure multiple parameters, this antenna is designed as a tri-frequency antenna to conduct measurements of different parameters at different frequencies. The antenna consists of three ELC resonators excited through the microstrip lines as shown in Fig. 1(a). The substrate is FR4, and the main material is copper. The ELC resonator serves as the sensing structure offering a simple design, low cost, and ease of miniaturization. In this structure, the central metal conductor acts as an inductor powered through the lower metal line, while the gaps at the left and right ends function as capacitors. The resonant frequency is calculated by the following formula:

$$f = \frac{1}{2\pi\sqrt{LC\varepsilon_r}} \tag{1}$$

where L represents the inductance, C is the capacitance, and ε_r denotes the relative dielectric constant of the material. By altering the width and length of the metal lines, the capacitance or inductance can be modified, thereby adjusting the center frequency. This allows for the creation of multiple resonant units with different frequencies.

Materials sensitive to light, humidity, and alcohol are applied by a drop-coating method onto the surfaces of resonator metal lines at different frequencies. For antennas coated with light-sensitive materials, light exposure causes electrons in the valence band of the photosensitive material to jump to the conduction band and become free electrons. Simultaneously, holes are formed in the valence band, leading to

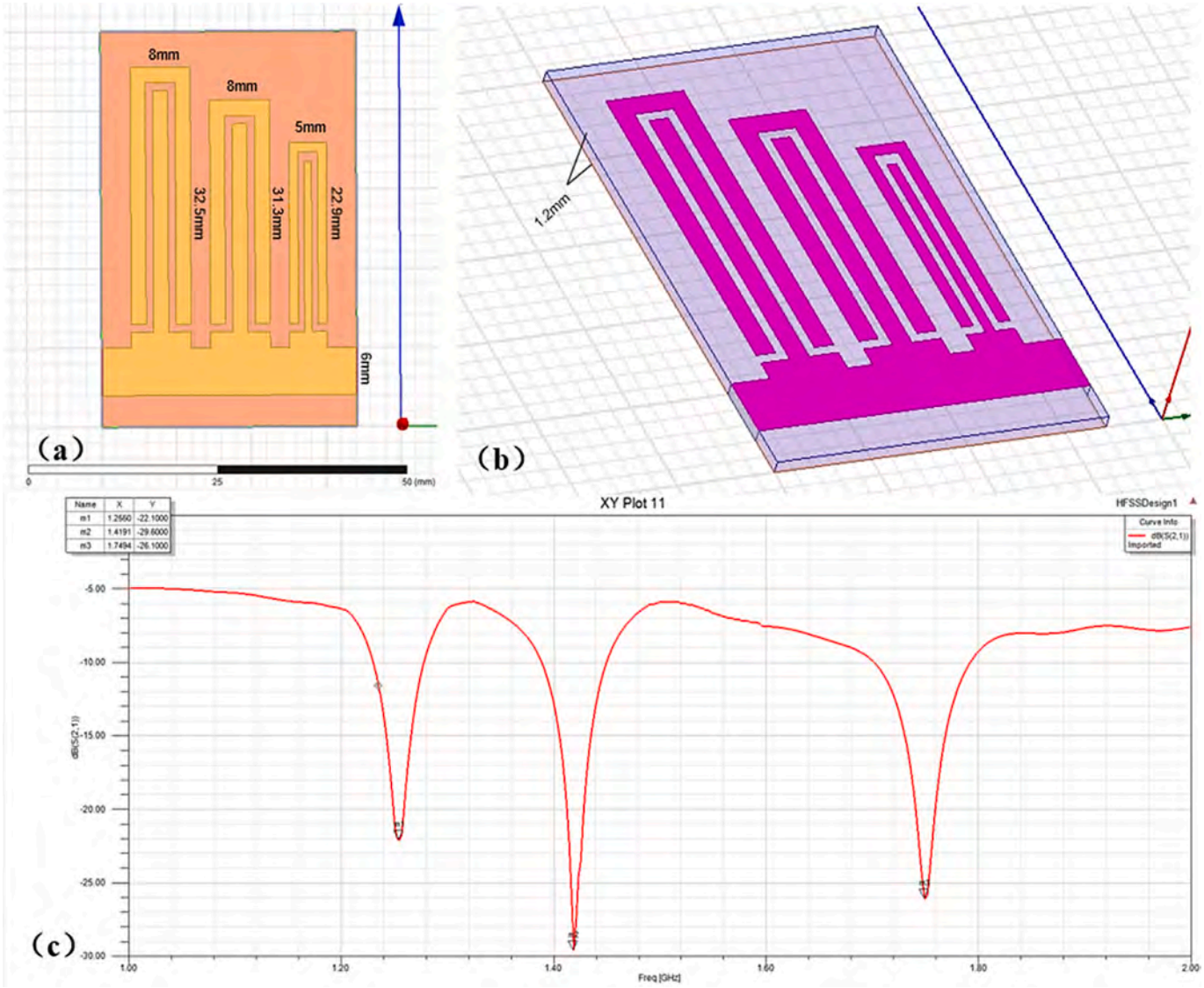

Fig. 1. (a) HFSS antenna design floor plan; (b) HFSS antenna design stereogram; (c) HFSS S21 parametric simulation plot.

changes in the resistance of the photosensitive material. This alteration affects the antenna impedance, subsequently causing variations in the center frequency or magnitude. For antennas coated with alcohol-sensitive materials, an increase in alcohol concentration in the environment leads to the adsorption of alcohol molecules on the surface of the alcohol-sensitive material. This alters the population of free electrons and produces changes in the resistance, subsequently affecting the antenna parameters. For antennas coated with humidity-sensitive materials, adsorption of water molecules onto the sensitive material causes changes in the dielectric constant thus influencing variations in the center frequency.

2.2. Simulation process

Based on the antenna concept, HFSS is utilized for antenna simulation and modeling. The substrate has a thickness of 0.7 mm and dimensions of 50 mm × 34.2 mm. Copper cladding is applied to the bottom of the substrate to serve as the antenna ground. On top of the substrate, a copper microstrip line is used and connected to the resonator, as illustrated in Fig. 1(b). When excited at one end, the ELC resonator absorbs the majority of the energy and resonates at certain specific frequencies to produce distinct valleys. Fig. 1(c) illustrates the S21 return losses at different frequencies of −22.1 dB, −29.6 dB, and −26.1 dB. Non-specific frequencies of incident waves are reflected, as observed in Fig. 2(a,b,c). The current density at the short end of the resonator and periphery of the U-shaped resonator is minimal at frequencies of 1.25 GHz, 1.41 GHz, and 1.75 GHz, indicating that the resonator primarily relies on coupling at the central position to influence the resonance frequency. By adjusting the length and width at the central position, the center frequency of the corresponding resonator can be altered. The Smith chart in Fig. 1(d) shows that the antenna impedance output at the respective frequencies complies with the 50 Ω impedance matching requirement, with a relatively small standing wave ratio, resulting in minimal reflection on the feed line and ensuring effective matching.

Fig. 2(e) shows that there is a slight disparity between the simulated S21 curve in HFSS and the actual measurement. This minor difference is primarily attributed to the idealized conditions assumed in the simulation involving ideal conductors, ideal insulators, and a vacuum environment. In practice, a reduction in frequencies is observed, mainly due to the inherent resistance in real conductors and non-ideal nature of insulators causing frequency variations. However, this subtle distinction does not significantly impact the antenna performance.

2.3. Fabrication validation

After optimizing the dimensions by HFSS simulation, the 3D model is exported from HFSS. Subsequently, the model is imported into Alium

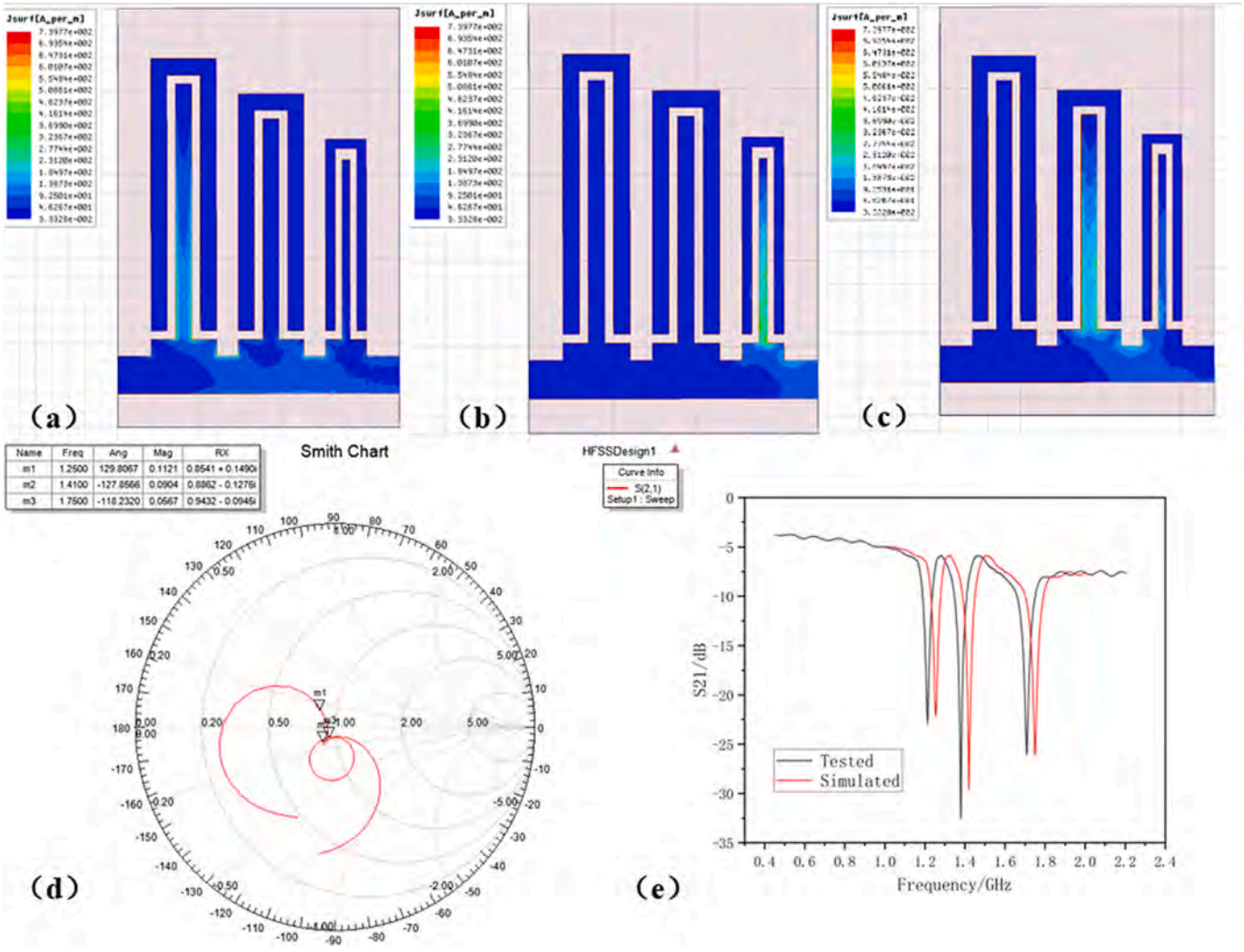

Fig. 2. **(a)** Current map excited by 1.25 Ghz; (b) Current map excited by 1.41 Ghz; (c) Current map excited by 1.75 Ghz; (d) Smith chart of the antenna; (e) Antenna simulation comparison.

Designer (AD), using an FR4 substrate with copper cladding for the antenna and ground sections to create the PCB model. Finally, the design is processed and manufactured by uploading it to the JLCPCB EDA platform. The advantage of this fabrication approach lies in the refined processes of large manufacturing facilities, resulting in antennas that closely match the simulation results together with relatively low costs and high repeatability.

3. Experimental design and details

3.1. Materials

The analytical grade chemicals included graphene oxide (GO), anhydrous ethanol (C2H5OH), glucose powder, copper nitrate hexahydrate ($Cu(NO_3)_2{\cdot}6H2O$), hexamethylenetetramine powder ((NH2CH2)4), sodium hydroxide powder (NaOH), ethylene glycol ($C_2H_6O_2$), tin(II) chloride dihydrate ($SnCl_2{\cdot}2H_2O$), zinc acetate ($Zn(CH_3COO)_2$), ammonium molybdate, and thiourea. The material, namely RGO, ZnO, SnO_2, CuO, and MoS_2, were prepared as shown in Fig. 3.

3.2. Preparation of sensor materials

The preparation process of RGO is as follows. Graphene oxide (GO, 50 mg) was placed in 10 mL of deionized water to form a dispersion by ultrasonic processing for 60 min. Anhydrous ethanol (40 mL) was added to obtain a 50 mL GO dispersion with a concentration of 1 mg/mL by sonication. The dispersion was placed in a magnetic stirrer, heated to 60 °C in a water bath for 60 min, and the glucose solution was added slowly during the process. After cooling to room temperature, the solution of reduced graphene oxide (RGO) was obtained and the steps are shown in Fig. 3(a).

A single-step hydrothermal process was employed to synthesize the pure ZnO powder. Briefly, 0.05 mmol zinc nitrate hexahydrate ($Zn(NO_3)_2{\cdot}6H2O$) and 1 mmol hexamethylenetetramine (HMTA) were mixed with 50 mL of deionized water and sonicated for 10 min. The mixture was transferred to a high-pressure autoclave lined with polytetrafluoroethylene (PTFE) and heated to 95 °C for 5 h. After cooling to room temperature, the white particles were washed with deionized water and dried at 60 °C for 30 min. The steps are shown in Fig. 3(b).

The preparation of SnO_2 is conducted by mixing tin (II) chloride dihydrate (0.45 g), sodium hydroxide (0.6 g), and 0.05 % zinc acetate. 15 mL of anhydrous ethanol and 15 mL of deionized water were mixed, sonicated in a beaker for 5 min, and stirred magnetically for 10 min. The solution was transferred to a high-pressure stainless-steel vessel lined with polytetrafluoroethylene (PTFE). The reaction proceeded at 180 °C for 24 h. After cooling, the tin dioxide powder was washed with anhydrous ethanol and dried in an oven at 60 °C as shown in Fig. 3(c).

CuO was prepared by putting 10 mL of 1.00 mol/L copper nitrate in 10 mL of the 1.00 mol/L sodium hydroxide solution. The hexamethylenetetramine powder (2 g) was added slowly under stirring. The same substrate was prepared with the same solution in triplicate. 15 mL of ethanol, ethylene glycol, and distilled water were added separately and stirred for 15 min to obtain a uniform solution. The solution was transferred to a high-pressure vessel lined with polytetrafluoroethylene (PTFE), reacted at 120 °C for 12 h, and cooled down to 20 °C at a rate of 10 °C/h. After cooling, the product was obtained by centrifugal separation in distilled water, washed with anhydrous ethanol, and dried in an oven at 50 °C. The steps are shown in Fig. 3(d).

The pure MoS_2 was prepared by putting 0.3 g of ammonium molybdate and 0.2 g of thiourea in 40 mL of deionized water and sonicated for 3 min. The transparent solution was then placed in a high-pressure reaction vessel lined with polytetrafluoroethylene (PTFE) and put in a muffle furnace. The temperature was raised to 180 °C, and the reaction proceeded for 24 h at this temperature. After cooling, the black precipitate was rinsed three times with anhydrous ethanol and deionized water to obtain the MoS_2 product. The cleaned MoS_2 was dried at 60 °C for 12 h to obtain the black and pure MoS_2 powder. The steps are shown in Fig. 3(e).

3.3. Preparation of sensors

The light sensor was prepared with the CuO/ZnO/RGO nanocomposite, the humidity sensor with the MoS_2/SnO_2/RGO nanocomposite, and the alcohol concentration sensor with the ZnO/MoS_2/RGO nanocomposite. 50 mg of CuO, 50 mg of ZnO, 50 mg of MoS_2, and 50 mg of SnO_2, were mixed in 10 mL of anhydrous ethanol and sonicated to obtain the CuO/ethanol dispersion, ZnO/ethanol dispersion, MoS_2/ethanol dispersion, and SnO_2/ethanol dispersion.

RGO has excellent electrical conductivity as well as a large surface area, which is suitable for the attachment and growth of other materials, resulting in better test sensitivity, so RGO is used as a substrate for the overcoating of materials in composites. The antenna was placed on a 60 °C heating platform. In the drop-casting method, RGO (30 μL) with good conductivity was placed uniformly on the metal wires of the three resonators of the antenna to form the first layer and dried. The coating with the sensitive material on top RGO provides a better response to the

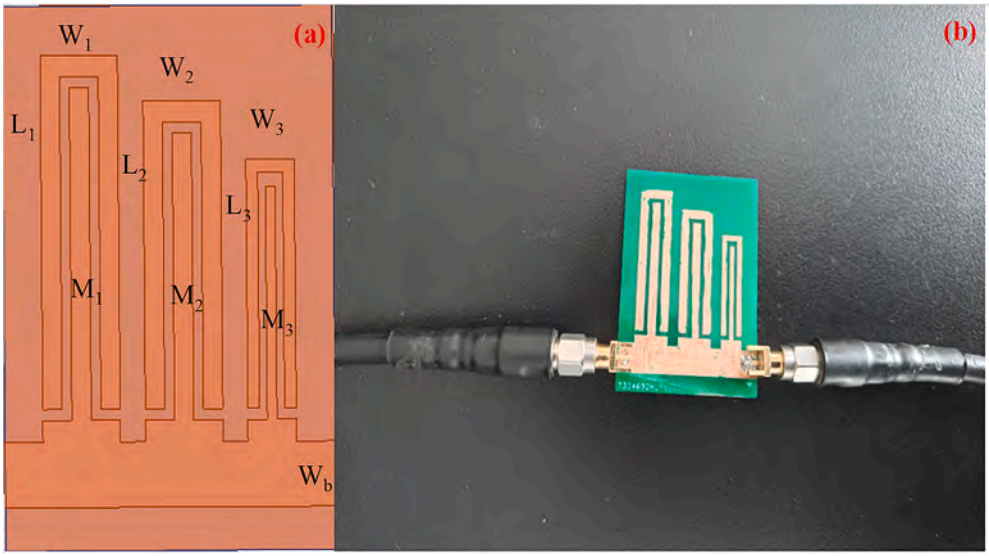

Fig. 3. Preparation of nano-sensitive materials by the hydrothermal method.

parameters resulting in better accuracy and performance. 30 μl of the ZnO/ethanol dispersion, 15 μl of the SnO_2/ethanol dispersion, and 20 μl of the MoS_2/ethanol dispersion were placed on the first layer of RGO on the three resonators and dried. 40 μl of the CuO/ethanol dispersion, 30 μl of the MoS2/ethanol dispersion, and 40 μl of the ZnO/ethanol dispersion were put on the second layer of the three resonators and dried.

These three different composite materials are coated on the surface of three different resonator microstrip lines to minimize the interference between the sensors and to achieve the purpose of testing three parameters at three frequency points separately.

4. Results and discussion

4.1. Characterization

SEM is performed on the CuO/ZnO/RGO nanocomposite as shown in Fig. 4(a). The floral structures in the image represent CuO, while the sheet-like structures correspond to graphene nanosheets and the rod-like structures adhering to them are ZnO. TEM is conducted on CuO/ZnO/RGO as shown in Fig. 4(b). In the TEM image, the larger floral structures correspond to CuO, the dark sheet-like structures represent graphene nanosheets, and the rod-like structures are ZnO. Both images illustrate the well-incorporated nature of ZnO nanorods adhering to both CuO and graphene nanosheets, demonstrating a homogeneous CuO/ZnO/RGO composite. The uniform integration of both materials enables better electron flow between them upon exposure to light, thereby enhancing the photosensitivity. The CuO/ZnO/RGO composite is analyzed by X-ray diffraction (XRD) as shown in Fig. 4(c). ZnO (JCPDS No.76–0704) exhibits diffraction peaks at 2θ of 31.736°, 34.378°, 36.214°, 47.483°, 56.534°, 62.775°, 67.866°, and 69.007°, corresponding to the crystallographic planes of (100), (002), (101), (102), (110), (103), (112), and (201), respectively. CuO (JCPDS No.89–5898) shows diffraction peaks at 2θ of 35.557°, 38.785°, 48.703°, 61.557°, and 66.220° associated with the crystallographic planes of (−111), (111), (−202), (−113), and (−311), respectively. RGO (JCPDS No. 89–8487) displayed a diffraction peak at 2θ of 26.554° indexed to the crystallographic plane of (002). X-ray photoelectron spectroscopy (XPS) is employed to determine the composition as shown in Fig. 4(d). The XPS spectrum unveils discernible peaks attributable to Zn $2p_3$, Cu $2p_3$, O 1 *s*, and C 1 *s*, imparting information about the chemical composition. The C 1 *s* spectrum in Fig. 4(e, exhibits peaks at 295.48 eV (C–C) and 287.68 eV (O-C = O), suggesting

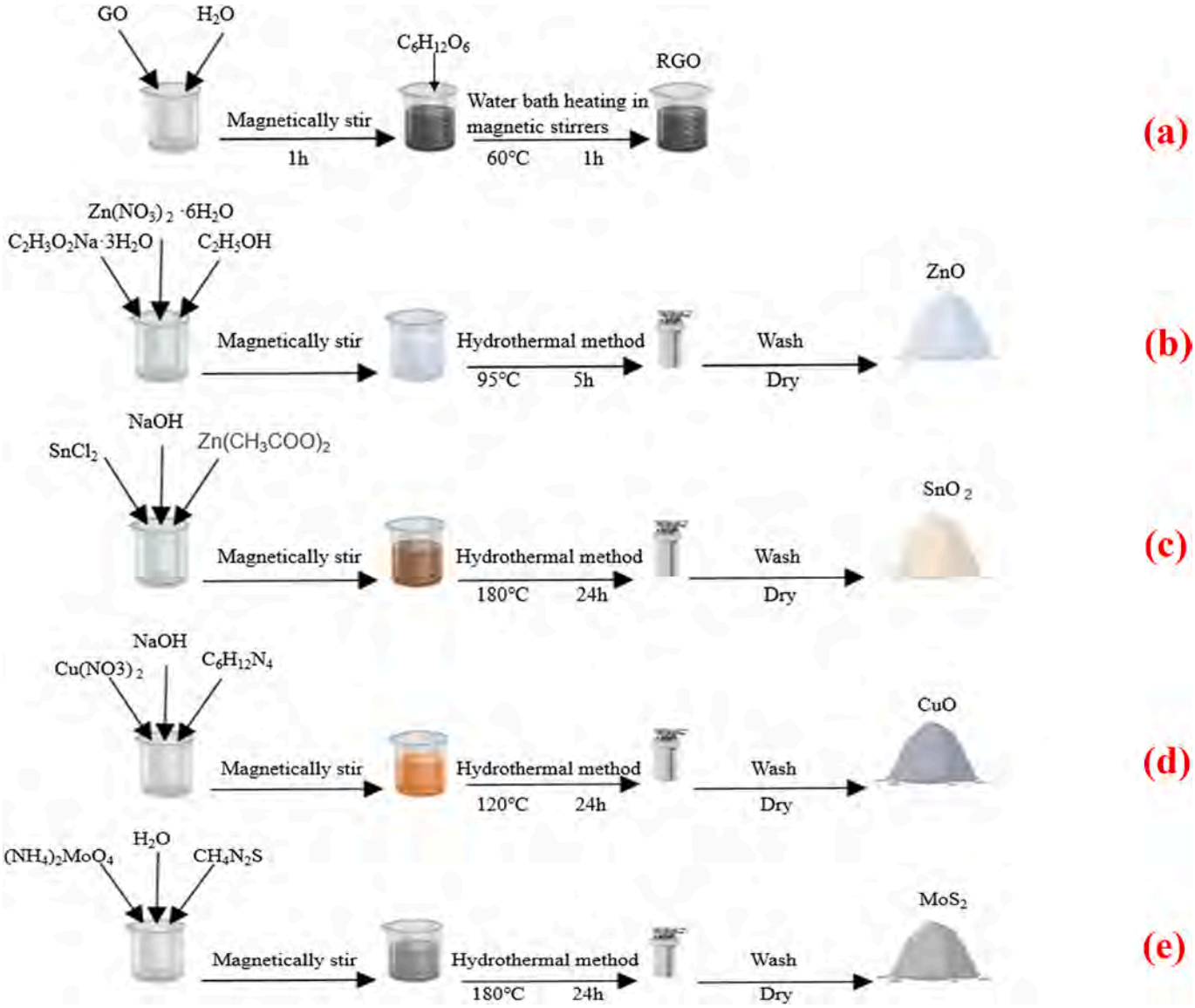

Fig. 4. (a) SEM characterization of ZnO/CuO/RGO; (b) TEM characterization of ZnO/CuO/RGO; (c) XRD characterization of ZnO/CuO/RGO; **(d)** XPS characterization of ZnO/CuO/RGO; **(e)** XPS C 1 *s* spectrum of ZnO/CuO/RGO.

the combination of RGO with oxide.

SEM and TEM are performed as shown in Fig. 5(a,b). The regularly aligned rod-shape ZnO structures intertwine with the spherical MoS_2 clusters, accompanied by an intermediate layer of sheet-like graphene nanosheets. When the MoS_2 or ZnO clusters are isolated, their close proximity hinders adsorption, resulting in reduced efficiency. As visually evident, the effective mixture of the two components successfully addresses the issue of excessive clustering. This synergistic combination enhances the adsorption of alcohol molecules to increase the transfer of ions in ethanol and improve the performance of alcohol detection. For a comprehensive analysis of the crystalline phases and constituent information of the ZnO/MoS_2/RGO composite, X-ray diffraction (XRD) is conducted as shown in Fig. 5(c). XRD reveals distinct peaks from MoS_2 (JCPDS No.74–0932) at 2θ of 37.968° and 51.284°, corresponding to the crystallographic planes of (104) and (018), respectively. RGO (JCPDS No.75–0444) exhibits diffraction peaks at 2θ of 26.309° and 54.105° corresponding to the crystal planes of (111) and (004), respectively. The crystallographic planes of ZnO is shown as aforementioned. X-ray photoelectron spectroscopy (XPS) is performed as shown in Fig. 5(d). The XPS spectra exhibit characteristic peaks corresponding to Zn 2p_3, Mo 3*d*, S 2p_1, O 1 *s*, and C 1 *s*. The C 1 *s* spectrum of the nanocomposite in Fig. 5(e) shows peaks at 284.98 eV (C–C), 285.68 eV (C-O), and 286.88 eV (O-C = O), indicating the formation of the incorporated graphene-based nanocomposite, which facilitates better interaction and reaction with alcohol molecules.

The SEM and TEM images are depicted in Fig. 6(a,b). By analyzing the morphological features on the microscopic scale, it is evident that numerous nanospheres of MoS_2, along with rod-shape SnO_2, adhere to the sheet-like graphene nanosheets. The surface of the nanosphere-shaped MoS_2 appears to be rough, resulting in an increased surface area that aids moisture absorption. Moreover, the rod-shape SnO_2, compared to the spherical shape, delivers superior performance in water absorption due to the larger surface area. SnO_2/MoS_2/RGO is analyzed by XRD, as shown in Fig. 6(c). The diffraction peaks of SnO_2 (JCPDS No. 71–0652) are observed at 2θ of 26.584°, 33.874°, 37.949°, and 81.752°, corresponding to the crystal planes of (110), (101), (220), and (400), respectively. XPS is used to analyze the elemental composition as well as chemical bonding, and Fig. 6(d) reveals peaks of O 1 *s*, Sn 3d_3, C 1 *s*, Mo 3*d*, and S 2p_1. The C 1 *s* spectrum in Fig. 6(e) shows peaks at 284.38 eV (C–C) and 285.98 eV (O-C = O) indicating a small amount of oxygen-containing functional groups and that RGO and SnO_2 exist in the nanocomplexes.

4.2. Sensing assessment and properties

Sequential tests are conducted on the sensors for light exposure, humidity, and ethanol concentration. The variations in S21 magnitude, response time, stability, and linear fitting are observed. To test the photosensitivity effect, the light intensity was adjusted by a solar simulator (SF300A-I/V), which varies the light intensity by voltage. Fig. 7(a) shows that the S21 data of the light-humidity-ethanol (LHE) sensor are collected in an indoor environment under constant conditions. In darkness, the S21 parameter is recorded at 22.9 dB. The light intensity from 9.7 klx to 39.1 klx results in a change in S21 from 30 dB to a maximum of 50.5 dB, with a sensitivity of 0.67 dB/klx and total variation of 20 dB. At the same time, the amplitude of the frequency points indicating humidity and ethanol gas concentration changed by only 1.7 dB and 1.5 dB respectively. Except for the subtle frequency deviations at 17.8 klx and below 9.7 klx in darkness, which are negligible due to the small magnitude, the change in the S21 amplitude is essentially linear with the light intensity. The S21 curve shows significant changes in both the frequency and magnitude when the environment transitions from darkness to illumination. In the absence of light, the sensitive material on the antenna remains inactive, resulting in a relatively high resistance. However, under illuminated conditions, the activation of the sensitive material leads to alterations in both the resistance and permittivity, thereby causing significant changes in the magnitude and frequency. Notably, these changes do not compromise the stability of the photometric measurements. The data are fitted as shown in Fig. 7(b) with a linear R^2 of 0.98966. The linearity of the antenna amplitude with illumination intensity is excellent. Specifically, under illumination of 25klx or below, the amplitude exhibits a nearly linear increase. However, as the illumination exceeds 25klx, a notable decrease in the rate of the amplitude change with light intensity is

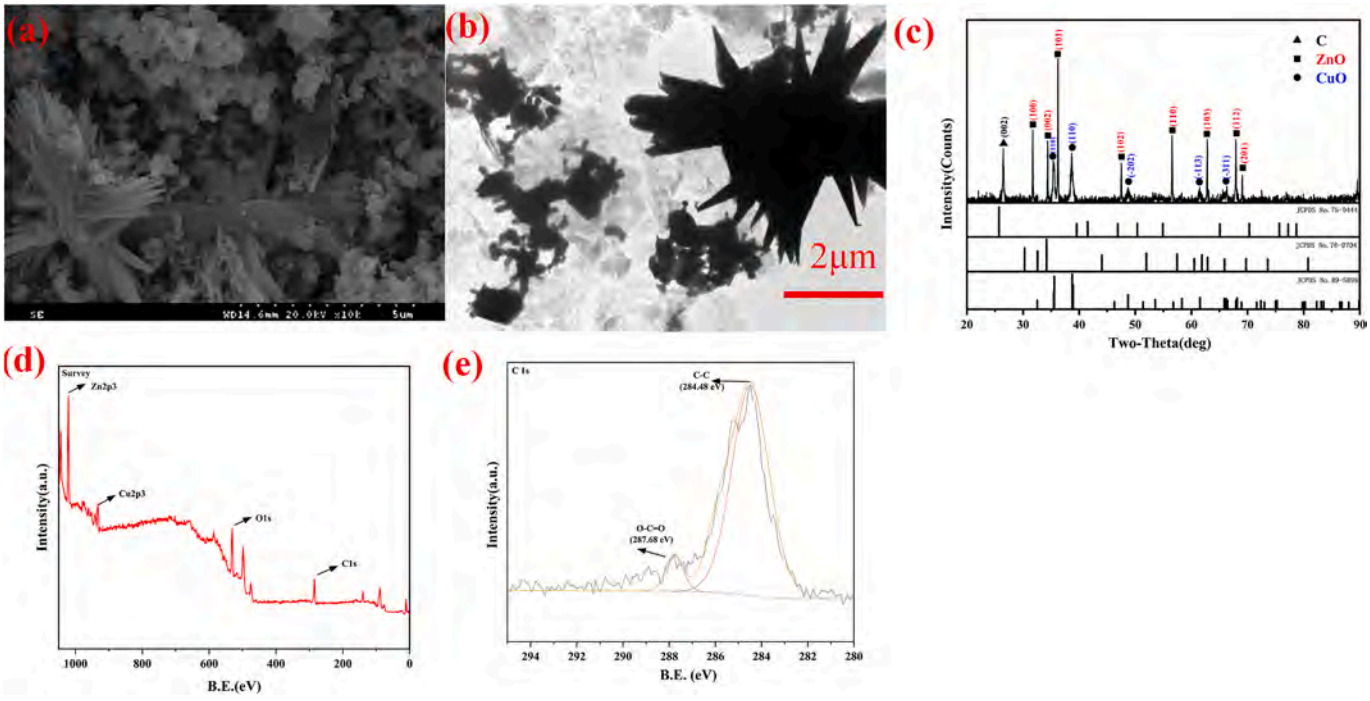

Fig. 5. **(a)** SEM characterization of MoS_2/ZnO/RGO; **(b)** TEM characterization of MoS_2/ZnO/RGO; **(c)** XRD characterization of MoS_2/ZnO/RGO; **(d)** XPS characterization of MoS_2/ZnO/RGO; **(e)** XPS C 1 *s* spectrum of MoS_2/ZnO/RGO.

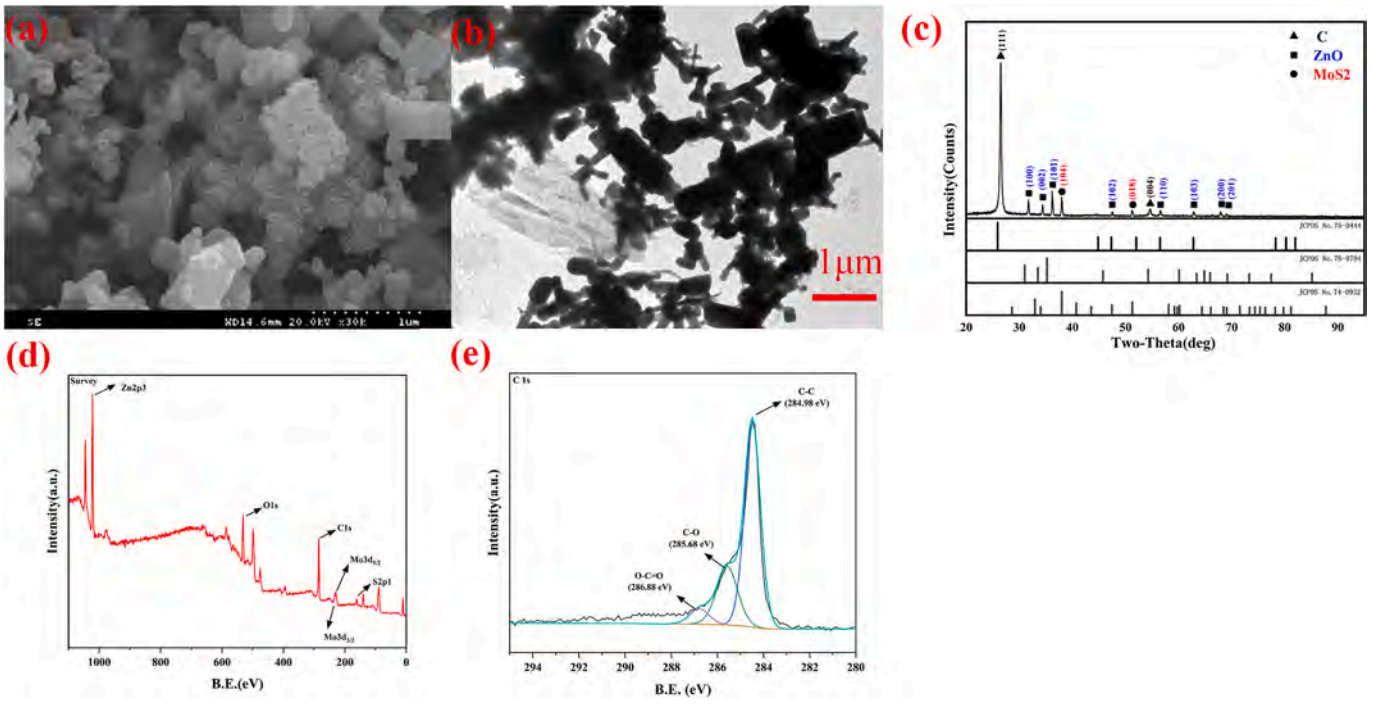

Fig. 6. **(a)** SEM characterization of SnO_2/ MoS_2/RGO; **(b)** TEM characterization of SnO_2/ MoS_2/RGO; **(c)** XRD characterization of SnO_2/ MoS_2/RGO; **(d)** XPS characterization of SnO_2/ MoS_2/RGO; **(e)** XPS C 1 *s* spectrum of SnO_2/ MoS_2/RGO.

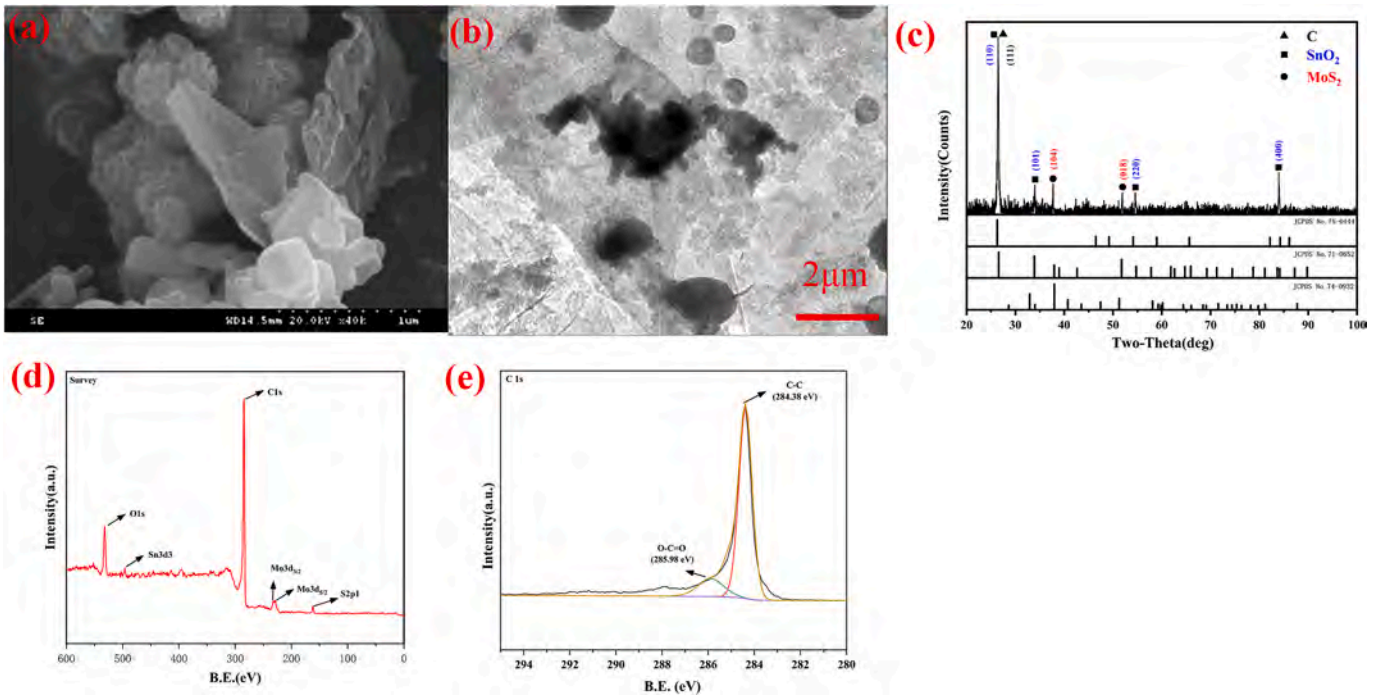

Fig. 7. **(a)** Effects of light intensity on the sensor **(b)** F-response diagram of the sensor; **(c)** Repeatability; **(d)** Stability.

observed to resemble a quadratic function. This indicates that at higher illumination intensities, the response of the composite approaches a threshold. Potentially, by increasing the material thickness or antenna area, satisfactory linearity may be achieved for high illumination intensities.

The stability is evaluated by maintaining the same light intensity for 30 min, as shown in Fig. 7(c). The S21 amplitude remains nearly constant, indicating good stability. The stability test under illumination with intensities ranging from 12.4klx to 31.6klx exhibits relatively good characteristics with minimal fluctuations. However, more significant fluctuations can be seen when the illumination intensity falls below 12.4klx or exceeds 31.6klx. The sensor performs optimally within the illumination intensity range of 12–31.6klx. These fluctuations occur within a relatively narrow range and do not compromise the accuracy of the measurements. Fig. 7(d) demonstrates the response time of the light sensor. After stabilizing the S21 curve in darkness, the solar simulator is

turned on with power adjustment to achieve a maximum light intensity of 39.1 klx. After stabilizing, the solar simulator is turned off and the process is repeated three times. The response time is determined to be 15.1 ± 0.7 s, and the recovery time is 25.2 ± 0.9 s. In real applications, the specific scenarios may require a controlled amount of light, while most conditions are typically dark. Given the high sensitivity of the sensor to light, particularly in transitions from darkness to illumination, the rapid response time is advantageous. In practical use, the rapid response allows for monitoring of light leaks and integrity of seals in breweries. Furthermore, in the light-exposure brewing stages, the sensor can assess whether appropriate light conditions are maintained and also provide real-time monitoring for timely adjustments.

In order to test the humidity, an airtight container is used, the humidity of the container is increased by a humidifier, and the real-time humidity of the container is detected by a humidity sensor, and the moisture is absorbed by a certain amount of calcium carbonate, thus controlling the humidity inside the container. As shown in Fig. 8(a), the humidity sensor is tested in the RH range from 20 % to 80 %. The S21 frequency decreases from 2.67 GHz to 2.47 GHz with a sensitivity of 2 MHz/% RH. Due to the adsorption of water molecules by the nanomaterials, there are minor offsets of 8 MHz and 6 MHz at other frequency points, attributed to slight influences on the dielectric constants of other materials, but these deviations can be considered negligible. As the humidity increases, both the frequency and amplitude change because the high humidity environment affects the impedance or permittivity of other parts of the antenna, resulting in amplitude variations. However, these changes do not compromise the accuracy of the measurements. As shown in Fig. 8(b), a linear fit an R^2 of 0.9771. At low humidity, a significant change in frequencies is observed when the humidity is between 20 % to 30 %. However, in the range of 40–80 % RH, the frequency remains relatively stable with good linearity. The overall measurement error is not particularly large. In the brewing industry, precise humidity detection is not required. Typically, the humidity during the brewing process remains above 40 % RH. Therefore, the measurement accuracy is suitable.

The stability is assessed by maintaining the same humidity for 30 min, as shown in Fig. 8(c). The frequency remains nearly constant demonstrating good stability. Fig. 8(d) shows the response time test, in which two airtight containers are employed. One container contains lime powder to reduce the humidity to 20 % RH, while the antenna is placed inside. After stabilizing the S21 frequency, the container is replaced by another containing a humidifier to raise the humidity to 80 % RH. This process is repeated three times. The humidity response time is 6.4 ± 0.5 s and the recovery time is 15.2 ± 0.8 s. The rapid response ensures better monitoring timeliness in breweries. The timely monitoring of humidity allows for real-time assessment of the brewing environment during the fermentation process and ensures that the conditions remain suitable for optimal brewing.

In order to test the concentration of ethanol gas, the container is first filled with ethanol gas, the ethanol sensor detects the concentration and excludes the gas way to control the concentration of ethanol gas. As shown in Fig. 9(a), the ethanol concentration sensor exhibits variations in the S21 gain from 35.4 dB to 17.5 dB in the concentration range of 0–1,800 ppm and a sensitivity of 0.01 dB/ppm. Meanwhile, the amplitude of the corresponding frequency of the antenna indicating light intensity and humidity varies only by 1.8 dB and 2.1 dB, respectively. The linear fit in Fig. 9(b) shows an R^2 of 9.5839. The amplitude linearity versus concentration is not ideal below 1,200 ppm showing relatively large errors. This stems from the uneven distribution of ethanol in the gas and inhomogeneous adsorption of ethanol at low concentrations. However, the linearity improves significantly above 1,200 ppm, and all the fluctuations fall within the acceptable error range. In practical brewing applications, the ethanol concentration is typically high. Fig. 9 (c) and 9(d) reveal consistent S21 amplitudes in the 30-minute test at the same concentration. Due to the inhomogeneous gas distribution, there are small fluctuations in the amplitude for the same concentration of ethanol. However, these fluctuations do not affect the sensing performance of the device. In the response time test, the container is filled with anhydrous ethanol vapor to displace air. The alcohol concentration is measured until 1,800 ppm. The sensor is then placed in the container, and after the S21 curve stabilizes, it is moved to an alcohol-free environment. This process is repeated three times and an average response time of 25.1 ± 1.2 s and recovery time of 41.6 ± 1.8 s are observed. The sensor thus has excellent stability and fast response for alcohol concentrations, especially at high-concentration environments.

The sensing performance of this design as well as the test dimensions show a significant improvement in response/recovery time compared to other sensors (see Table.1).

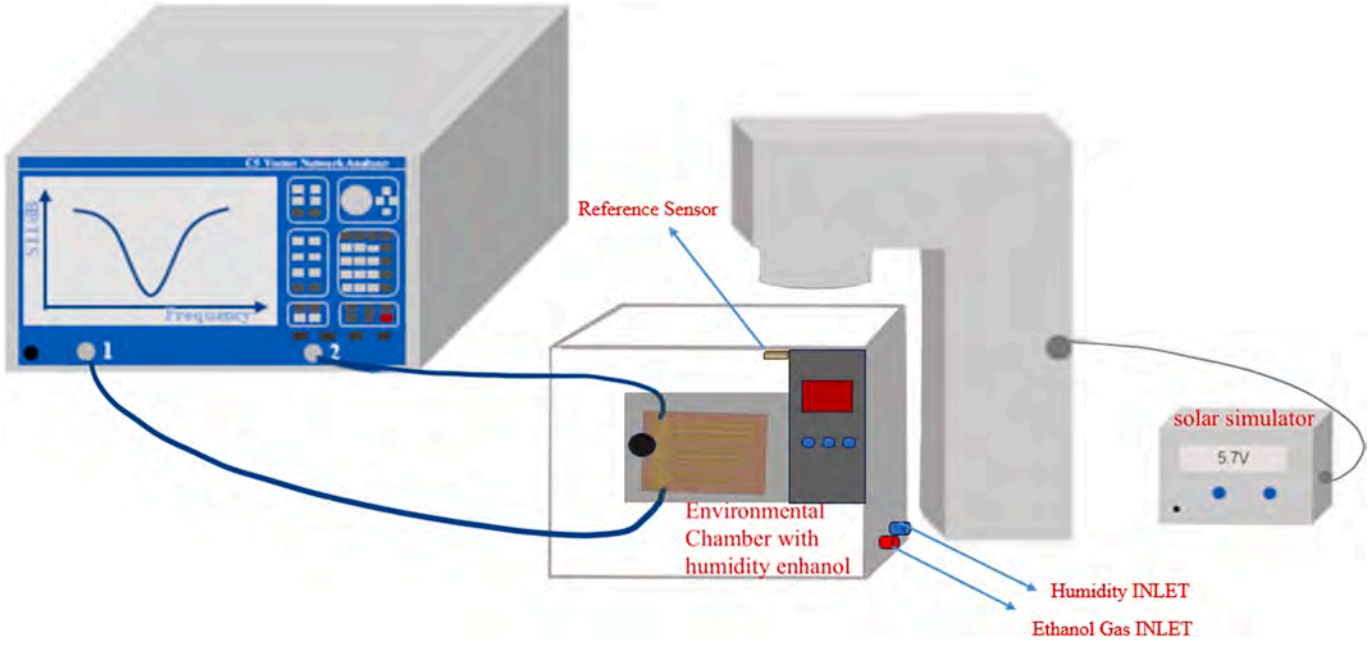

Fig. 8. **(a)** Effects of humidity on the sensor; **(b)** F-response diagram of the sensor; **(c)** Repeatability; **(d)** Stability.

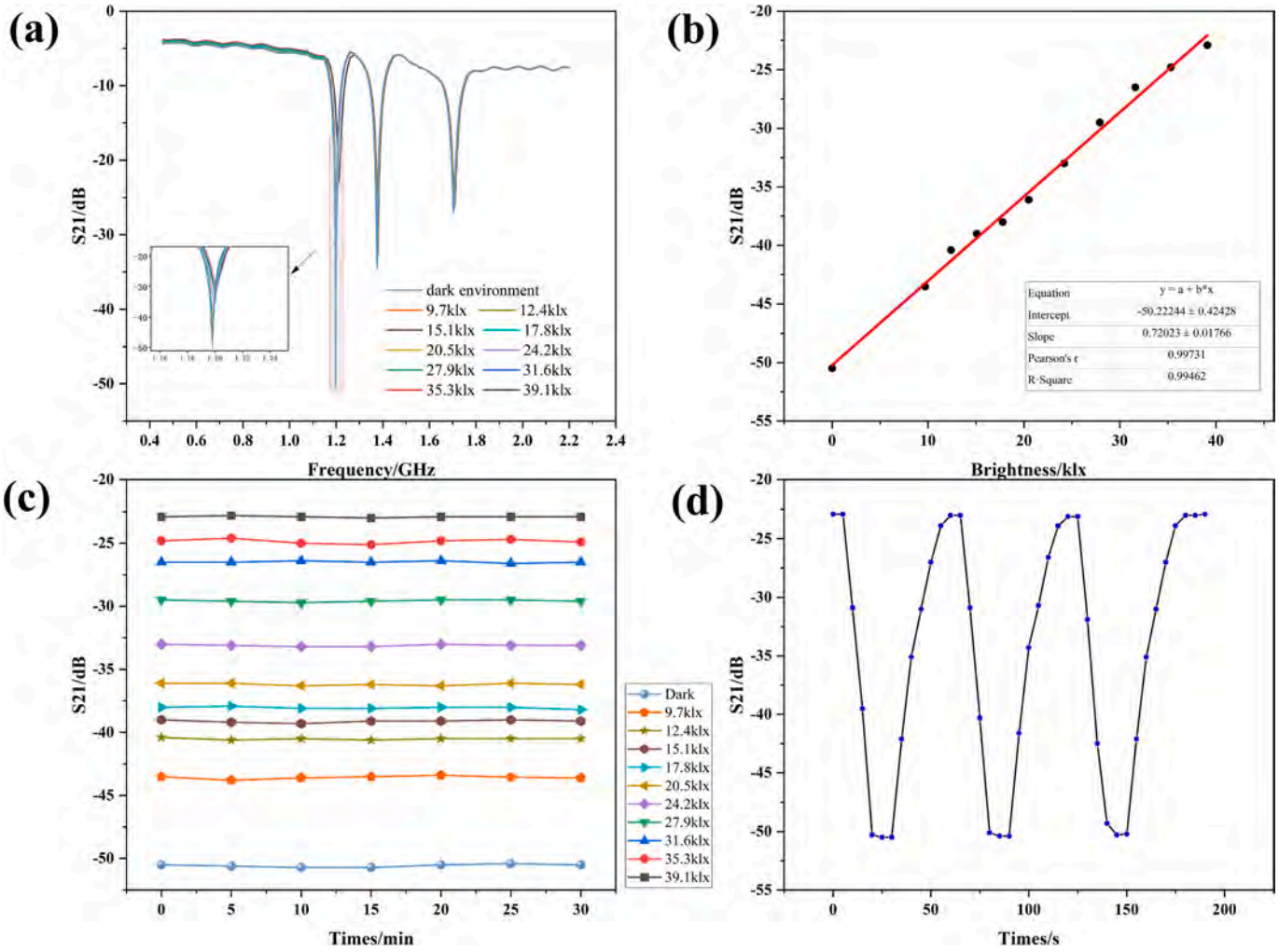

Fig. 9. **(a)** Effects of alcohol concentrations on the sensor; **(b)** F-response diagram of the sensor; **(c)** Repeatability; **(d)** Stability.

Table 1
Comparison with other sensors.

Materials	Cost	Test Range	Res/Rec Time	Refs.
ND/CNC	high	11–97 % RH	19/3	[27]
N3-loaded ZnO nanocluster	low	0–2000 ppm	63.2 / 21.5	[28]
CNCs	low	11–97 % RH	60/15	[29]
ZnO nanowalls/Ag	low	–	10/81	[30]
CuO/ZnO/RGO	low	9.7–39.1 klx	15/25	This work
MoS2/SnO2/RGO		20–80 % RH	7/15	
ZnO/MoS2/RGO		0–1800 ppm	25/41	

4.3. Sensing mechanism

In the band structure of CuO, oxygen atoms form mainly covalent bonds with copper ions (Cu2 +) due to the higher electronegativity of oxygen. CuO acts as a p-type semiconductor, where the copper ions are prone to losing electrons. Upon illumination, electrons from the valence band of CuO are excited to the conduction band, forming electron-hole pairs and increasing the number of charge carriers in the valence band. On the other hand, ZnO, as an n-type semiconductor, undergoes excitation upon illumination, where electrons from the valence band are excited to the conduction band to generate free electrons. The interface between CuO and ZnO forms a p-n junction, leading to changes in resistance upon illumination, thereby affecting the parameters of the antenna. The reaction mechanism is illustrated in Fig. 10(a).

Ethanol molecules exhibit reducing properties. As zinc oxide (ZnO) is an n-type semiconductor, it harbors a significant population of free-moving electrons on its surface. Oxygen molecules in air can capture some of these electrons to generate various forms of oxygen ions such as O_-, O^{2-}, and O_2^-. This results in the depletion layer on the surface of ZnO and a smaller concentration of charge carriers as well as higher resistance in air. Meanwhile, owing to the spherical characteristics, MoS_2 provides more effective adsorption sites to facilitate the capture of ethanol and oxygen molecules. This setup is conducive to the reaction between ethanol and these ions, resulting in additional electrons and a higher concentration of free electrons, thereby altering the carrier concentration and the impedance of the antenna. The reaction mechanism is illustrated in Fig. 10(b).

Nanomaterials such as MoS_2 and SnO_2 adsorb water molecules from the environment. Water molecules, being polar, exhibit a noticeable electric dipole moment due to the stronger electronegativity of the oxygen atom and the weaker electronegativity of the hydrogen atom in water molecules. This induces the polarization and increases the dielectric constant to alter the parameters of the antenna. The mechanism of the reaction is shown in Fig. 10(c).

5. Conclusion

A passive RFID sensor for multidimensional environmental monitoring is designed for automated processes in breweries. The sensor simultaneously monitors three key parameters: illumination, humidity, and alcohol concentration in air. The antenna model is designed and

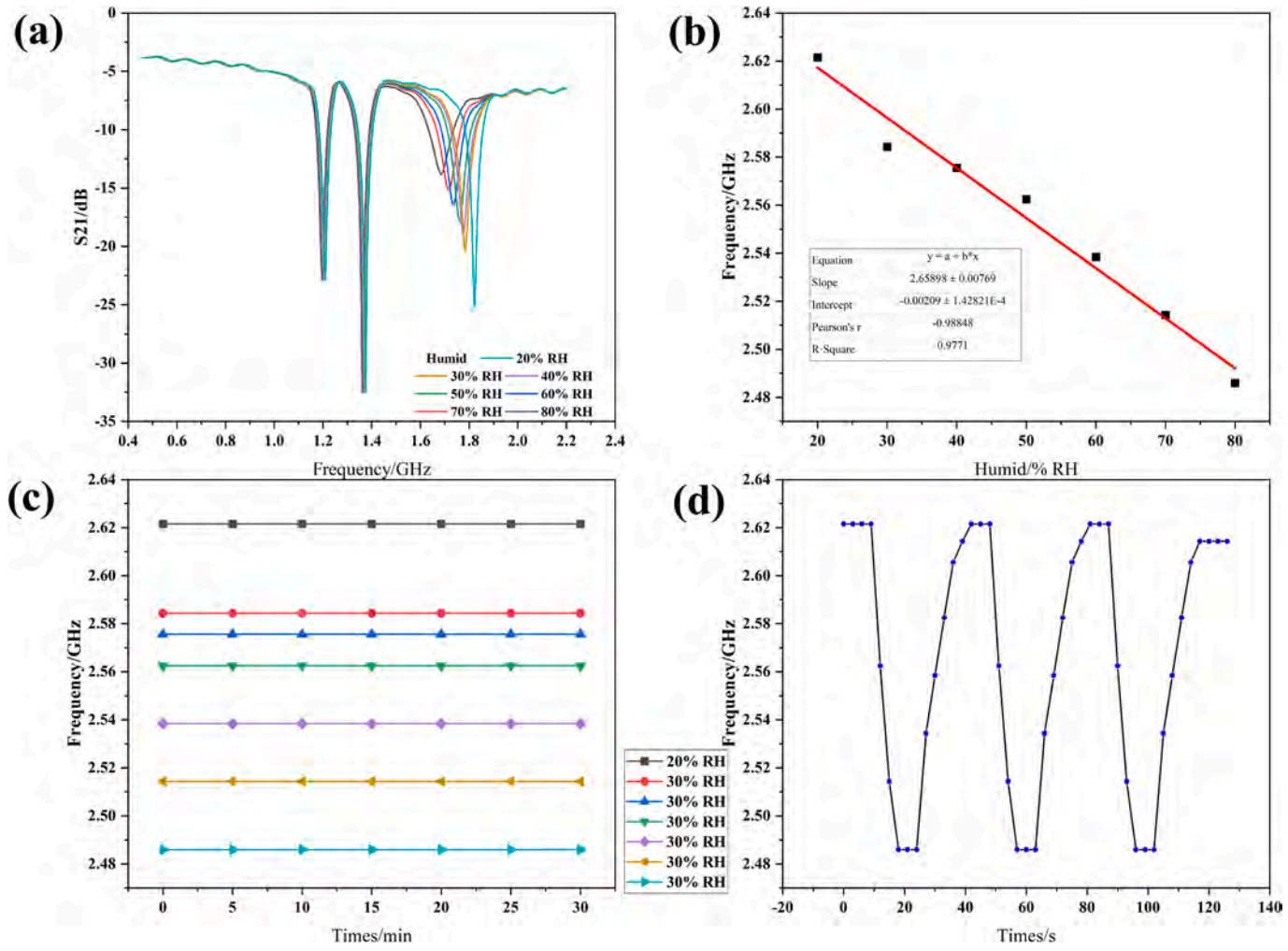

Fig. 10. **(a)** Light intensity sensitivity mechanisms; **(b)** Ethanol sensing mechanism; **(c)** Humidity sensing mechanism.

optimized for dimensions and performance by HFSS simulation. The final model is translated into a PCB enabling cost-effective and straightforward manufacturing. The sensitive nanomaterials are prepared by a hydrothermal method which is economical and simple. The passive RFID multidimensional sensor delivers stable monitoring performance ranging from 9.7 to 39.1 klx in illumination, 20–80 % RH in humidity, and 0–1800 ppm in alcohol concentration. Under ambient conditions, the sensor exhibits a sensitivity of 0.67 dB/klx for light, 2 MHz/%RH for humidity, and 0.01 dB/ppm for alcohol concentration. The response and recovery times are 30 s, 20 s, and 50 s, respectively, and high repeatability and stability are demonstrated. Each parameter is determined based on the amplitude or frequency change at specific frequencies, resulting in minimal mutual interference and allowing simultaneous and accurate measurement of multiple parameters in complex environments. Experimental results confirm that the passive RFID sensor for multidimensional environmental monitoring can measure three parameters simultaneously. The strategy and sensor have significant potential in monitoring large-scale automated brewing processes and prospects in other types of commercial and laboratory monitoring.

CRediT authorship contribution statement

Bairui Tao: Funding acquisition, Conceptualization. **Linxin Dong:** Writing – original draft, Data curation. **Fengjuan Miao:** Supervision, Resources, Project administration. **Xiao Liang:** Writing – review & editing. **Paul K. Chu:** Writing – review & editing.

Declaration of competing interest

The authors declare that they have no known competing financial interests or personal relationships that could have appeared to influence the work reported in this paper.

Acknowledgments

We would like to thank the Engineering Research Center of Agricultural Multi-Dimensional Sensor Information Perception, Heilongjiang Province, and Heilongjiang Provincial Key Laboratory of Micro-Nano Sensor Component. This work was jointly supported by the graduate innovation project of Qiqihar University (No. YJSCX2022027), Fundamental Research Funds in Heilongjiang Provincial Universities (No.145309802), Heilongjiang Science Foundation Project (No. LH2023F052), Heilongjiang Province University Discipline Collaborative Innovation Achievement Project (No. LJGXCG2023-070), City University of Hong Kong Strategic Research Grant (SRG No. 7005505), and City University of Hong Kong Donation Research Grants (Nos. DON-RMG 9229021 and 9220061).

Ethical approval

This article does not contain any studies with human participants or animals performed by any of the authors.

Data availability

Data will be made available on request.

References

[1] Z. Meng, Y. Liu, N. Gao, et al., Radio frequency identification and sensing: integration of wireless powering, sensing, and communication for IIoT innovations, IEEE Commun. Magaz. 59 (3) (2021) 38–44.

[2] F. Costa, S. Genovesi, M. Borgese, et al., A review of RFID sensors, the new frontier of internet of things, Sensors 21 (9) (2021) 3138.

[3] F. Vivaldi, B. Melai, A. Bonini, et al., A temperature-sensitive RFID tag for the identification of cold chain failures, Sensors Actuat. A Phys. 313 (2020) 112182.

[4] M. Bhattacharjee, F. Nikbakhtnasrabadi, R. Dahiya, Printed chipless antenna as flexible temperature sensor, IEEE Internet Things J. 8 (6) (2021) 5101–5110.

[5] Z. Duan, Y. Jiang, H. Tai, Recent advances in humidity sensors for human body related humidity detection, J. Mater. Chem. C 9 (42) (2021) 14963–14980.

[6] H. Yu, C. Wang, F.Y. Meng, et al., Design and analysis of ultrafast and high-sensitivity microwave transduction humidity sensor based on belt-shaped MoO3 nanomaterial, Sensors Actuat. B Chem. 304 (2020) 127138.

[7] R. Rayhana, G. Xiao, Z. Liu, RFID sensing technologies for smart agriculture, IEEE Instrument. Measurem. Magazine 24 (3) (2021) 50–60.

[8] M. Wagih, A.S. Weddell, S. Beeby, Battery-free wireless light-sensing tag based on a long-range dual-port dual-polarized RFID platform, Sensors 22 (13) (2022) 4782.

[9] W. Ran, L. Wang, S. Zhao, et al., An integrated flexible all-nanowire infrared sensing system with record photosensitivity, Adv. Mater. 32 (16) (2020) 1908419.

[10] G. Shi, X. Shen, Y. He, et al., Passive wireless detection for ammonia based on 2.4 GHz square carbon nanotube-loaded chipless RFID-inspired tag, IEEE Trans. Instrum. Measurem. 72 (2023) 1–12.

[11] C.A. Zito, T.M. Perfecto, A.C. Dippel, et al., Low-temperature carbon dioxide gas sensor based on yolk–shell ceria nanospheres, ACS Appl. Mater. Interf. 12 (15) (2020) 17745–17751.

[12] R. Feng, Y. Chang, L. Mao, et al., Liquid pressure sensing system with coupling RFID and HMM based on distance measurement, IEEE Sensors Journal 21 (2) (2020) 1051–1058.

[13] R. Colella, M.R. Tumolo, S. Sabina, et al., Design of UHF RFID sensor-tags for the biomechanical analysis of human body movements, IEEE Sensors Journal 21 (13) (2021) 14090–14098.

[14] S.K. Behera, Chipless RFID sensors for wearable applications: a review, IEEE Sensors Journal 22 (2) (2021) 1105–1120.

[15] C. Occhiuzzi, S. Parrella, F. Camera, et al., RFID-based dual-chip epidermal sensing platform for human skin monitoring, IEEE Sensors J. 21 (4) (2020) 5359–5367.

[16] P. Yang, Y. Feng, J. Xiong et al. Rf-ear: contactless multi-device vibration sensing and identification using cots rfid. IEEE INFOCOM 2020-IEEE Conference on Computer Communications. IEEE, 2020: 297-306.

[17] S.H. Min, H.J. Kim, Y.J. Quan, et al., Stretchable chipless RFID multi-strain sensors using direct printing of aerosolised nanocomposite, Sensors Actuat. Phys. 313 (2020) 112224.

[18] S. Ahmad, R. Khosravi, A.K. Iyer, et al., Wireless capacitive liquid-level detection sensor based on zero-power RFID-sensing architecture, Sensors 23 (1) (2022) 209.

[19] V. Mulloni, A. Gaiardo, G. Marchi, et al., Sub-ppm NO2 detection through chipless RFID sensor functionalized with reduced SnO2, Chemosensors 11 (7) (2023) 408.

[20] I. Ali, A.E.H.B. Kashyout, M. Tayel, et al., Ruthenium (Ru) doped zinc oxide nanostructure-based radio frequency identification (RFID) gas sensors for NH3 detection, J. Mater. Res. Technol. 9 (6) (2020) 15693–15704.

[21] S. Dey, R. Bhattacharyya, S.E. Sarma, et al., A novel "smart skin" sensor for chipless RFID-based structural health monitoring applications, IEEE Internet Things J. 8 (5) (2020) 3955–3971.

[22] S. Qiu, H. Zhao, N. Jiang, et al., Multi-sensor information fusion based on machine learning for real applications in human activity recognition: state-of-the-art and research challenges, Inform. Fus. 80 (2022) 241–265.

[23] F. Requena, N. Barbot, D. Kaddour, et al., Combined temperature and humidity chipless RFID sensor, IEEE Sensors Journal 22 (16) (2022) 16098–16110.

[24] F. Mirlou, L. Beker, Wearable electrochemical sensors for healthcare monitoring: a review of current developments and future prospects, IEEE Trans. Mol. Biol. Multi-Scale Commun. 9 (3) (2023) 364–373.

[25] J. Yeo, J.I. Lee, Y. Kwon, Humidity-sensing chipless RFID tag with enhanced sensitivity using an interdigital capacitor structure, Sensors 21 (19) (2021) 6550.

[26] P.K. Varshney, A. Kapoor, M.J. Akhtar, Highly sensitive ELC resonator based differential sensor, IEEE Trans. Instrument. Measurem. 70 (2021) 1–10.

[27] Q. Chen, K. Mao, Y. Yao, et al., Nanodiamond/cellulose nanocrystals composite-based acoustic humidity sensor, Sensors Actuat. B Chem. 373 (2022) 132748.

[28] Q. Wang, J. Hong, Z. Zhang, et al., Visible light-activated ethanol sensor based on flower-like N3-loaded ZnO composites, Sensors Actuat. B Chem. 370 (2022) 132399.

[29] Y. Yao, X. Huang, B. Zhang, et al., Facile fabrication of high sensitivity cellulose nanocrystals based QCM humidity sensors with asymmetric electrode structure, Sensors Actuat. B Chem. 302 (2020) 127192.

[30] C. Li, H. Kan, J. Luo, et al., A high performance surface acoustic wave visible light sensor using novel materials: Bi 2 S 3 nanobelts, RSC Adv. 10 (15) (2020) 8936–8940.